Mechanics and Fracture of Structured Pillar Interfaces

Simon Heide-Jørgensen^{c,a}, Michal K. Budzik^{a,b,*}, Kevin T. Turner^c

^a Mechanical Engineering Section, Department of Engineering, Aarhus University, Aarhus, Denmark

^biMAT - Centre for Integrated Materials Research, Aarhus, Denmark ^cDepartment of Mechanical Engineering and Applied Mechanics, University of Pennsylvania, Philadelphia, PA, USA

Abstract

Material architecture and geometry provide an opportunity to alter the fracture response of materials without changing the composition or bonding. Here, concepts for using geometry to enhance fracture resistance are established through experiments and analysis of the fracture of elastic-brittle, polymer specimens with pillar-structures along the fracture plane. Specifically, we investigate the fracture response of double cantilever beam specimens with an array of pillars between the upper and lower beams. In the absence of pillars, unstable crack growth and rapid catastrophic failure occur in the double cantilever specimens tested in displacement control. Introducing pillars at the interface by removing material via laser cutting yields a discontinuous interface and leads to a more gradual fracture process and an increase in the work of fracture. The pillar geometry affects the failure load and, notably, increasing the slenderness of the pillars leads to higher critical failure loads due to greater load sharing. The effect of pillar geometry on

^{*}Corresponding author

 $^{{\}it Email~addresses:}~ {\tt mibu@eng.au.dk}~({\tt Michal~K.~Budzik~}),~ {\tt kturner@seas.upenn.edu}~({\tt Kevin~T.~Turner})$

fracture is established through experiments and analysis, including analytical modeling and finite element simulations. An analytical model that includes the macro-scale response of the beam and the micro-scale response of the pillars is presented and describes the key effects of pillar geometry on fracture response.

Keywords: Mechanical metamaterials, architected materials, toughness, heterogeneities, finite element analysis

1. Introduction

High stiffness, strength and toughness are desired properties of materials in structural applications. While obtaining two of the three properties simultaneously, e.g. stiffness and toughness (e.g. elastic-ductile materials) or strength and stiffness (e.g. ceramics) are rather easy, achieving high strength, toughness and stiffness is challenging [4]. For instance, increasing the strength can lead to brittleness, which reduces toughness and damage tolerance. Controlling the internal geometry can potentially assist in achieving all three properties simultaneously by altering the fracture process, failure modes, or crack growth paths. Especially, for brittle materials affecting the critical unstable crack growth can enhance damage tolerance. Mechanical metamaterial is a class of materials in which mechanical properties are determined by the internal geometry of the material rather than by the composition or atomic bonding. Lattice materials are common examples [34, 40, 25] and have gained attention due to their exceptional properties, notably high stiffness per weight. The advances in mechanical metamaterials in recent years have been driven by progress in digital manufacturing techniques that allow for fabrication of materials with complex internal geometry via additive, subtractive and selective manufacturing processes [46, 45, 10, 42, 48, 53, 35, 39, 18]. Mechanical analysis and simulation have been equally important providing the ability to design internal geometry and architecture to realize specific properties. The use of geometry has also received substantial interest from the adhesion community where geometrical features have been exploited to control toughness of interfaces [49, 15, 5, 24, 37, 12, 47]. One outcome of the work to design dry adhesives with high adhesion strength is an adhesion scaling law [8], which suggests that the critical fracture force is proportional to the square root of the ratio between system compliance and contact area. This law was recently revisited and generalized to account for the case of progressive failure [36].

The objective of this work is to understand the fracture behavior of structured interfaces consisting of an array of pillars. The high-level goal is to identify strategies to improve the toughness of the material through geometric control. We fabricated, tested, and analyzed structured double cantilever beam (DCB) specimens including symmetric geometries where the pillar region is subjected mainly to the uniaxial loading (i.e. mode I) and asymmetric geometries with a small contribution of in-plane shear stress (i.e. mixed-mode I/II) to failure. Through laser cutting of elastic-brittle Plexiglas[®] (i.e. PMMA) sheets the slenderness of the pillars is varied systematically while their intermediate distances are kept constant. The specimen behavior is analyzed using comprehensive analytical formulation and finite element analysis. Good agreement between the analytical model, experimental results, and numerical simulations is reported. More specifically, we detail the relationship

between the long-range structural response of the specimen and the shortrange micro-mechanical response of the pillar structure. The results indicate that the pillar-like geometries can be used to increase the critical fracture load and improve damage tolerance while minimally affecting the stiffness. Due to the geometrical nature of the enhancements, the conclusions are expected to remain valid over a range of different length scales and, therefore, be relevant for a number of different applications. Potentially, new or additional insights can be gained into: fracture in polymers via crazing and fibrillation phenomena, i.e. slender micro-structures with negligible bending stiffness, which could benefit from the load sharing mechanism [14, 38, 17]; the role of geometrical parameters in fracture of composites incorporating fibre bridging [50, 51]; nature inspired material architectures [13, 26, 21, 1]. The results may provide insight into more complex, truss-like, structures [44, 28, 29] and their behavior within confined or constrained zones of multi-materials including load transfer in sandwich materials with lattice-like cores. Finally, further directions toward adhesive bonding toughening can be deduced [32, 33].

2. Materials and methods

2.1. Specimen

DCB specimens with a total length $L=160 \,\mathrm{mm}$, a load application point 10 mm from the end, width $b=3 \,\mathrm{mm}$, lower beam thickness of $h=20 \,\mathrm{mm}$, and top beam thickness of 20 or 30 mm were examined (Fig. 1). The specimens were laser cut (flatbed laser cutter, 10.6µm wavelength, CO₂ gas, 40W laser used at 80% power, 10mm min⁻¹ speed, Ten High, China) from 3 mm thick, extruded sheets of poly(methyl methacrylate) (PMMA) with a Young's

modulus of $E^* \approx 2.7 \,\text{GPa}$, Poisson's ration $\nu = 0.33$ (adopted from product data sheet) and a fracture energy of $\mathcal{G}_c \approx 0.25 \,\text{N}\,\text{mm}^{-1}$ (see Appendix A1 for details on material property determination). Three types of specimens were tested: 1) reference PMMA DCB specimens; 2) DCB specimens with a pillar-like pattern along the interface (referred to as symmetric specimens) and 3) DCB specimens with a thicker top beam and a pillar-like pattern along the interface (referred as asymmetric specimens).

The reference [used mainly to estimate the fracture energy of PMMA (see Appendix A1) and symmetric specimens had $h = 20 \,\mathrm{mm}$ for both the top beams and bottom while the asymmetric specimens had a top beam of thickness 30 mm, yielding a top-to-bottom thickness ratio of $\alpha = 30/20 = 1.5$. Both, symmetric and asymmetric specimens had, if not stated otherwise, an initial crack length $a = 90 \,\mathrm{mm}$ as defined in Fig. 1(a). The pillars constituting the bondline had a constant width d=1 mm, a constant spacing of $s = 1 \,\mathrm{mm}$, while their height was varied: $t = 1, 3, 5, 9 \,\mathrm{mm}$. For each pillar height, three specimens for a total of twelve were manufactured and tested. To control the crack and ensure failure at the interface between the two substrates, the laser cutter (35 % power, $100 \,\mathrm{mm \, s^{-1}}$) was used to etch a line of approximately 250 µm depth [measured using a 3D scanning macroscope (Keyence VR3200, Japan) along the middle of the specimen (Fig. 2). To relieve stress concentrations at the base of the pillars, fillets of $R \approx 200 \,\mu\text{m}$ were introduced. Failure originating from the corners was not observed during the experiments.

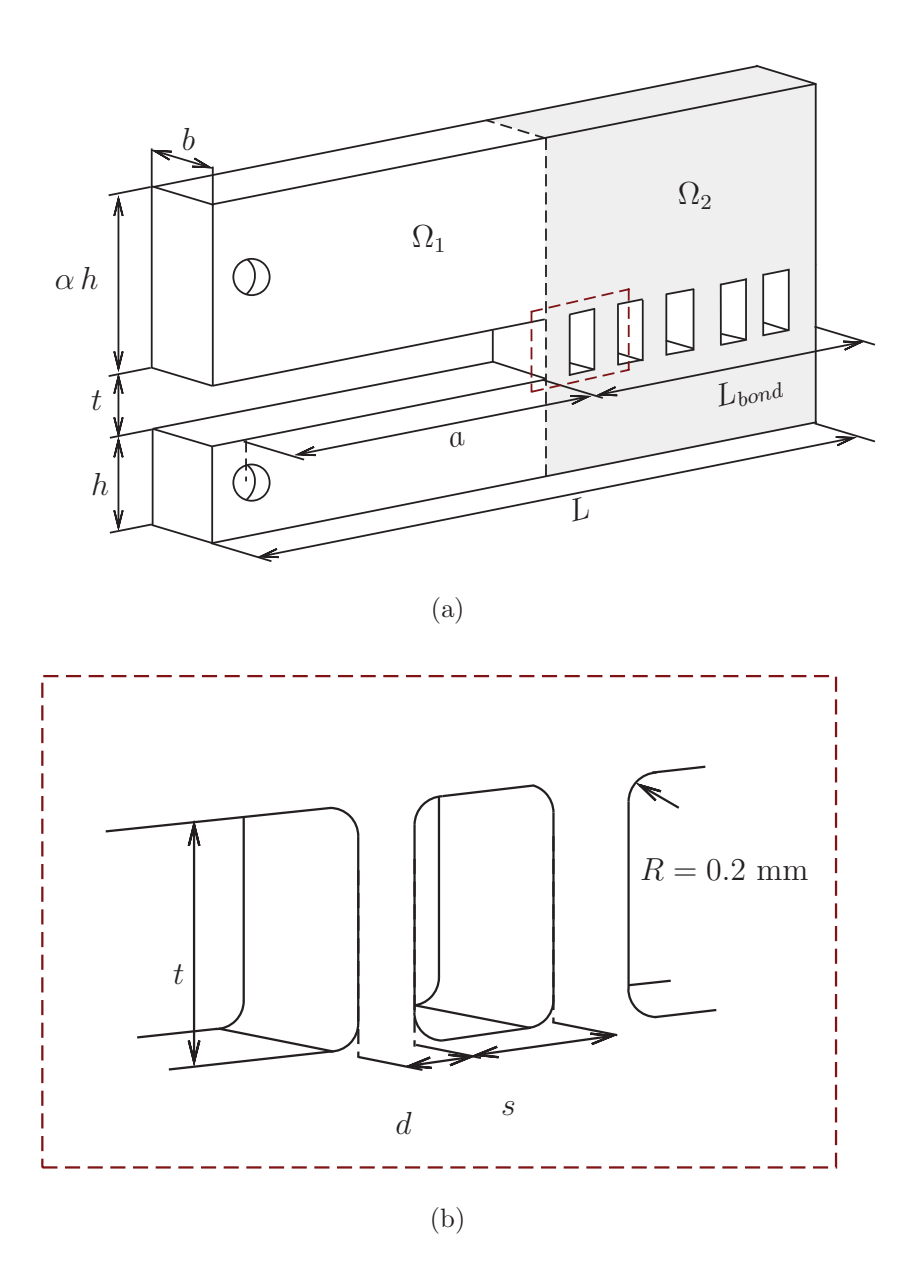


Figure 1: Schematic of the specimens with unbonded region Ω_1 and bonded region Ω_2 . a) Specimen dimensions comprising length L, width b, initial crack length a, bonded length L_{bond} , beam thickness h, pillar height t and top-to-bottom thickness ratio α . b) Close-up of the pillars at the bondline with, width d and spacing s.

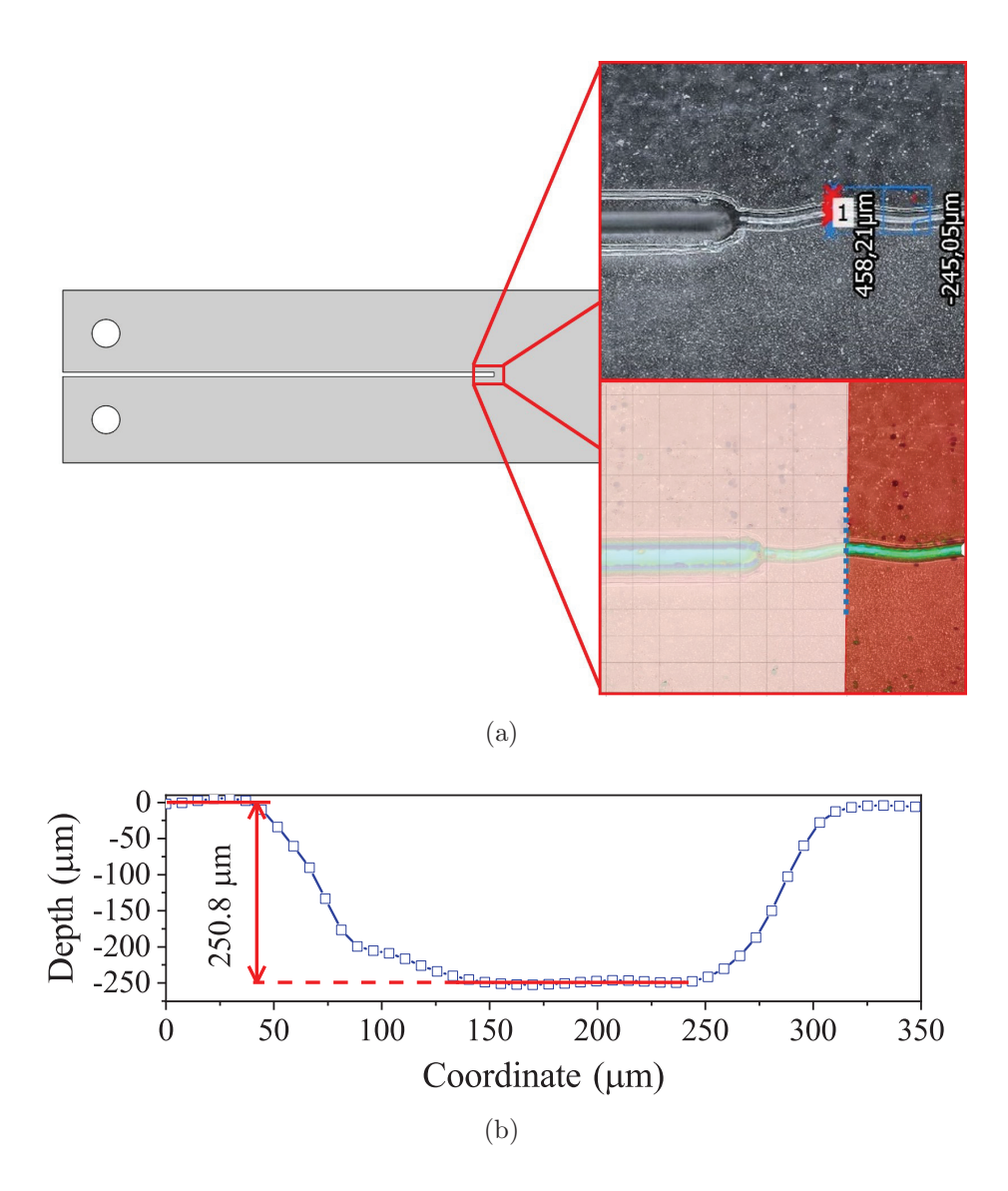


Figure 2: Image and measured profile of the crack tip of the reference specimen. a) Region of interest marked on a schematic of the reference specimen. The two close-up images show, from top to bottom, an optical image of the crack tip region with the etched line and a topographic measurement of the same area. b) Height profile along the dashed, blue line in a). The depth of the etched trench is approximately 250 µm.

2.2. Testing

Each specimen was mounted using custom-made grips in a universal testing machine (Zwick/Roell Z050, Zwick/Roell, Germany). The tests were performed at a constant displacement rate of 3 mm min⁻¹. Crosshead and force data were acquired simultaneously at a rate of 50 Hz.

3. Finite Element Analyses

A finite element analysis of the specimen geometries was programmed in Python (v. 2.7.3, Python Software Foundation) and solved using Abaqus (Abaqus/CAE 18.21.41, Dassault Systèmes, France). The geometry is modeled using four-noded, plane strain elements (plane strain conditions are assumed, since for most of the cases the relevant non-dimensional group of parameters: b/d; $t/d \approx 1$) with reduced integration and a linear elastic, isotropic material model. The model and mesh are depicted in Fig. 3.

The top and bottom beams are modeled separately and connected with a surface-to-surface contact along the interface. The lower loading point is fixed and a load is applied to the upper loading point. During post-processing, the displacement at loading point and the stresses σ_{yy} and σ_{xy} at the middle of the pillars, as indicated by the thick line in Fig. 3, are obtained. The mesh density in the pillar region is higher compared to the rest of the model. A convergence study showed that it is feasible to use a global mesh seed of 0.5 mm and a local mesh seed of 30 µm for the pillars. This provided a maximum of 732,530 elements in the model and 33 elements across the width of each each pillar.

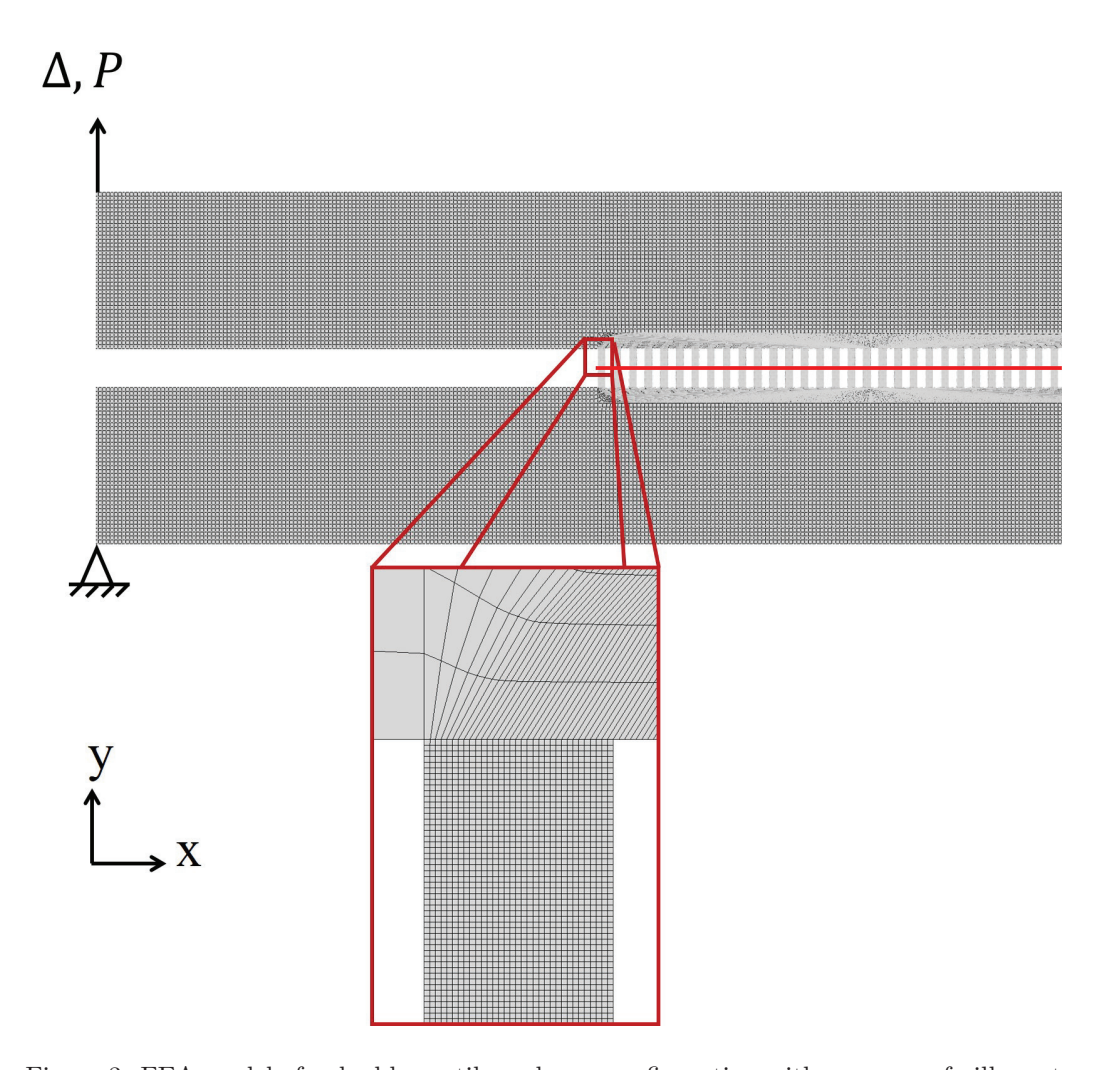


Figure 3: FEA model of a double cantilever beam configuration with an array of pillars at the interface. The close-up of the first pillar shows details of the mesh. The configuration is loaded at the end with Δ while the reaction force, P, is acquired at the same point. Stresses, σ_{yy} and σ_{xy} , are extracted along the interface denoted by the red line.

4. Theoretical Framework

4.1. Macro-Mechanical Model

The focus of this section is on developing a relatively simple and intuitive model for interpretation of the macroscopic behavior of the specimen in terms of substrate properties and effective interface properties of the pillar region. This approach neglects the geometrical details of the interface by treating it as homogeneous with spatially averaged properties.

The model is assumed to be under a prescribed force, P, loading, however, this is easily changed to a prescribed displacement if required. For the beams, Timoshenko theory is used while the pillar interface is represented as a Winkler foundation - recently reviewed [16]. Use of a beam theory framework that includes shear to represent the beam is deemed necessary due to the beam aspect ratio $\min(a/h) = 6$ for which the internal shear effects cannot be neglected. The Winkler foundation that describes the interface region cannot account for shear stresses, however, allows the model to remain simple and intuitive.

The model (Fig. 1) is then divided into two regions 1) the free/unbonded region (Ω_1) and the interface/bonded region (Ω_2), both connected through continuity conditions.

The equilibrium equations of the Timoshenko beam on the Winkler foundation [43] are:

$$\frac{dM}{dx} + V = 0 \qquad \qquad \frac{dV}{dx} - kw = 0 \tag{1}$$

with:

$$M = EI_{\beta} \frac{d\varphi}{dx}$$
 $V = \kappa GA_{\beta} \left(\frac{dw}{dx} - \varphi\right)$ with $\beta = t, b$ (2)

where M, V, w, and k are bending moment, shear force, deflection, and foundation modulus, respectively, and $\varphi, E, I_{\beta}, \kappa, G$, and A_{β} are rotation, elastic modulus, moment of inertia, shear coefficient, shear modulus, and the cross-sectional area, respectively. The subscript β either takes t for top or b for bottom such that $I_t = (\alpha h)^3 b/12$ and $I_b = h^3 b/12$. For a rectangular, homogeneous and isotropic beam the cross-sectional area, shear coefficient and shear modulus are $A_{top} = \alpha hb$ and $A_{bot} = hb$, $\kappa \approx 5/6$ [52], and $G = E/2(1 + \nu)$ with ν being the Poisson's ratio.

4.1.1. Interface Region Homogenization

Instead of a discrete formulation of the interface [22], which would lead to over-complicated derivation, at present this region is regarded as continuous with a representative unit cell consisting of a pillar with length d and a spacing of length s. The foundation modulus is taken as the resulting stiffness of the unit cell:

$$k = \left(\frac{2b}{t}E_{pillar}\right)f + \left(\frac{2b}{t}E_{spacing}\right)(f-1) = \left(\frac{2b}{t}E\right)f \tag{3}$$

Such formulation can be used within a general context, for instance including material variability [32, 33]. In the present study $E_{pillar} = E$, $E_{spacing} = 0$ and f = d/(d+s). Thus, k defines a homogenized stiffness of the pillar region. Defining $E = mE^*$ where m is a constant, allows for adaptation of different stress-strain states [23]. m = 1 for plane stress and

 $m=(1-\nu^2)^{-1}$ for two-dimensional plane strain. Following the FEA, the latter assumption is used throughout the paper.

4.1.2. Unbonded Domain

The unbonded domain spans from the load application point (x = 0) to the crack tip (x = a), with subscript $()_1$ referring to quantities in this domain. Within the domain k = 0. With bending moment, M = -Px and shear force, V = -P, integration of eq. (2) yields:

$$\varphi_1 = \int -\frac{P}{EI_\beta} x dx = -\frac{P}{2EI_\beta} x^2 + A_1 \tag{4}$$

where A_1 is a constant of integration. Combining eqs. (2) and (4) and integrating leads to:

$$w_1 = \int \frac{P}{\kappa G A_{\beta}} + \frac{P}{2EI_{\beta}} x^2 + A_1 dx = \frac{P}{6EI_{\beta}} x^3 + \frac{P}{\kappa G A_{\beta}} x + A_1 x + B_1$$
 (5)

where B_1 is an additional constant of integration. Both constants are found by imposing deflection and rotation continuity at the crack tip.

4.1.3. Intact Domain

The intact domain representing the interface region spans from the crack tip (x = a) to the end of the specimen (x = L) with $k \neq 0$.

The governing equation for a Timoshenko beam on an elastic foundation is:

$$\frac{d^4w}{dx^4} - \frac{k}{\kappa G A_\beta} \frac{dw^2}{dx^2} + \frac{k}{E I_\beta} w = 0 \tag{6}$$

with a solution of the form:

$$w_2 = A_2 e^{-\gamma_1 x} + B_2 e^{\gamma_1 x} + C_2 e^{-\gamma_2 x} + D_2 e^{\gamma_2 x}$$
(7)

 A_2, B_2, C_2 and D_2 are unknown constants. γ_1 and γ_2 are the roots of the eigenvalue problem eq. (6) given by:

$$\gamma_1 = \lambda \sqrt{2\left(\varepsilon + \sqrt{\varepsilon^2 - 1}\right)}$$
 $\gamma_2 = \lambda \sqrt{2\left(\varepsilon - \sqrt{\varepsilon^2 - 1}\right)}$
(8)

with λ and ε being phenomenological parameters related to the elastic process zone of the foundation's damping of the beam deflection [22] and to the modulation of the damping to either periodic or monotonic decay [43], respectively. They are expressed as:

$$\lambda = \sqrt[4]{\frac{k}{4EI_{\beta}}} \qquad \varepsilon = \frac{\sqrt{k EI_{\beta}}}{2\kappa GA_{\beta}} \tag{9}$$

The rotation, obtained by combining eqs. (2) and (7) and integrating, gives:

$$\varphi_2 = -\psi_1 A_2 e^{-\gamma_1 x} + \psi_1 B_2 e^{\gamma_1 x} - \psi_2 C_2 e^{-\gamma_2 x} + \psi_2 D_2 e^{\gamma_2 x}$$
(10)

where ψ_1 and ψ_2 are constants depending on the geometry and the material of the specimen:

$$\psi_1 = \frac{\kappa G A_{\beta} \gamma_1^2 - k}{\kappa G A_{\beta} \gamma_1} \qquad \psi_2 = \frac{\kappa G A_{\beta} \gamma_2^2 - k}{\kappa G A_{\beta} \gamma_2}$$
(11)

Constants A_2 and C_2 are determined through rotation and shear angle continuity between the two domains. The remaining constants, $B_2 = D_2 = 0$, are found by assuming the far field as intact $(w_2 = 0, \phi_2 = 0 \text{ as } x \to \infty)$.

4.1.4. Strain Energy Release Rate

The compliance is calculated as ratio of the total displacement of the top and bottom beams to the applied force:

$$C = \frac{w_1(\beta = t) + w_1(\beta = b)}{P} \bigg|_{x=0}$$
(12)

The strain energy release rate (SERR) for the macro-mechanical configuration is obtained by combining eq. (12) and the Irwin-Kies equation, which states

$$\mathcal{G} = \frac{P^2}{2b} \frac{dC}{da} \tag{13}$$

Assuming that the crack grows once the Griffith fracture criterion [20] is satisfied, eq. (13) is set equal to the critical strain energy release rate, \mathcal{G}_c , and an expression for the critical force, P_c , i.e. force necessary for crack onset, is obtained:

$$P_c = \sqrt{2b\mathcal{G}_c}\sqrt{\frac{da}{dC}} \tag{14}$$

Note, that the adhesion scaling law [8], in a generalized form [36], i.e. $P_c \propto \sqrt{\frac{dA}{dC}}$ with dA = bda, is recovered. Griffith's criterion requires the material to behave in an elastic-brittle manner, though small scale yielding is also allowed [30]. With the relatively small dimensions of the pillars (t,d) this can be questioned. The critical material length scale can be associated with the size of the crack tip plastic zone calculated as: $r_p = c \frac{\mathcal{G}_{Ic}E}{\sigma_y^2}$ where $c \in (\frac{1}{2\pi}; \frac{\pi}{8})$ [41]

depending on the assumed stress-strain conditions. For PMMA it equates to $r_p \approx 10^1 \, \mu \text{m}$. From dimensional analysis following non-dimensional groups are recognized: $\frac{r_p}{t}$; $\frac{r_p}{d}$; $\frac{r_p}{R}$. Here, $\frac{r_p}{R}$ is the largest with a magnitude on the order of 10^{-1} . The others are on the order of 10^{-2} or lower. We conclude, that in the present case the material can be regarded as brittle.

4.2. Micro-Mechanical Concepts

In the previous section, the pillar region was treated as homogeneous, thus a dependence on pillar geometry was not obtained from the analysis. The geometrical realization of the concept of tunable toughness must be related to the distance between the pillars and the pillar aspect ratio. Additional, independent, non-dimensional groups could appear as important: $\frac{t}{d}$; $\frac{s}{d}$. The presence of a gap between the pillars alters the load transfer and introduces new mechanisms of failure. Fig. 4 shows a schematic view of the kinematic field experienced by pillars at the interface. Only the top adherend and the region near the adherend/first pillar is considered. In the general case, the adherends are of different bending rigidities, thus the top and bottom sections of the specimen will experience different rotations and displacements. The following assumptions are made: $\frac{1}{2}(\delta - t)/d = (\phi_t - \phi_b)t$ and $\lambda \cdot d \ll 1$. With the notation of Fig. 4, the loading distributed over the pillars can be separated into two distinct cases: 1) tension/compression of the pillars following $(\delta - t) = (w_t + w_b)$ (for the geometries studied compressive failure was not observed, however, for completeness analysis of the associated failure mode can be found in Appendix A2) and 2) shear through $u = (\phi_t - \phi_b)t$.

With the proposed load decomposition it is assumed that the failure mechanism of a single pillar is representative for the overall failure of the specimen.

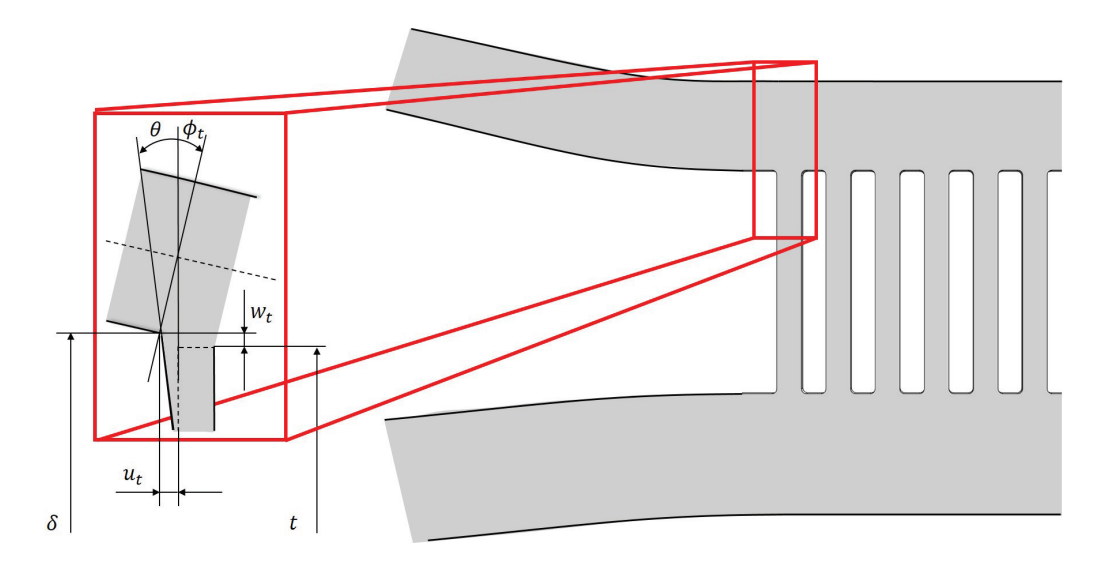


Figure 4: Schematic representation of the kinematic field of the first pillar. Only the top pillar-beam transition is shown for clarity (denoted with index t).

4.2.1. Pillars Under Mode I Loading

Tension of the pillar results in uniaxial force P_p and produces a moment M_p (with subscript p referring to the pillar). The mechanism of energy dissipation is through fracture caused by loads P_p and M_p . The change in elastic energy stored in the first pillar from P_p reads as:

$$\Delta U_p = \frac{1}{2} \sigma(x = a) \varepsilon \Delta V = \frac{1}{2} \frac{\sigma^2}{E} \Delta V$$
 (15)

where we define $\sigma = \frac{P_p}{A_p}$ and $\varepsilon = \frac{\sigma}{E}$ assuming average values of both stress and strain. Here $A_p = b d$ is the cross sectional area of the pillar while ΔV is the volumetric change of the pillar between the loaded and the unloaded stages, i.e. $\Delta V = A_p \Delta \delta$. Combining previous equations we obtain:

$$\Delta U_p = \frac{1}{2} \frac{P_p^2}{A_p E} \tag{16}$$

The displacement $\Delta \delta$ is eliminated using the axial stiffness of the pillar $(k_p = EA_p/t)$, resulting in:

$$\Delta U_p = \frac{1}{2} \frac{P_p^3 t}{A_p^2 E^2} \Delta \delta \tag{17}$$

Following a similar approach the stored elastic energy due to the moment is:

$$\Delta U_m = \int_0^b \int_{-d/2}^{d/2} \frac{1}{2} \frac{\sigma^2}{E} dx dy \Delta \delta = \frac{6M_p^2 \Delta \delta}{E d^3 b}$$
 (18)

where we define $\sigma = x \frac{M_p}{I_p}$ with $I_p = d^3b/12$. Again, $\Delta \delta$ is eliminated using the stiffness of the pillar and eq. (18) is rewritten as:

$$\Delta U_m = \frac{6M_p^2 P_p t}{d^3 b E^2 A_p} \tag{19}$$

With the elastic energy defined, the energy release rate is given as the change of elastic energy with the change of crack area:

$$\mathcal{G}_{tens} = \frac{(\Delta U_p + \Delta U_m)}{\Delta A_p} \tag{20}$$

Assuming that there exists a crack a_p such that $A_p = b(d - a_p)$ leads to:

$$\mathcal{G}_{tens} = \frac{1}{4} \frac{P_p^3 t}{(d - a_p)^3 b^3 E^2} + \frac{3M_p^2 P_p t}{d^3 b^3 E^2 (d - a_p)^2} = \mathcal{G}_p + \mathcal{G}_m$$
 (21)

Within the limit of $a_p \to 0$, which sets up $P = P_c$ we obtain:

$$\mathcal{G}_{ctens} = \frac{1}{4} \frac{P_p^3 t}{d^3 b^3 E^2} + \frac{3M_p^2 P_p t}{d^5 b^3 E^2} \tag{22}$$

Moreover, taking $P_p = \sigma b d$ and $M_p \approx P_p (d+s)$ yields:

$$\mathcal{G}_{ctens} = \left[\frac{1}{4} \left(1 + \frac{s}{d} \right)^3 + 3 \left(1 + \frac{s}{d} \right)^5 \right] \left(\frac{t}{d} \right) \left(\frac{\sigma^3 d}{E^2} \right) \tag{23}$$

A complex relation between the pillars hight, the width, the spacing and the SERR is revealed. The spacing-to-width ratio s/d increases the SERR while the aspect ratio t/d decreases the SERR.

4.2.2. Shear Loading of Pillars

Under the shear loading applied to the specimen, a single pillar can be treated as a cantilever beam under loading of the force $P_{\tau} = \int_{0}^{d} \tau(x)b \, dx$. Using Timoshenko beam theory, the compliance is:

$$C_p = \frac{u}{P_\tau} = \frac{t^3}{3EI_p} + \frac{2t}{\kappa A_p G} \tag{24}$$

where $I_p = \frac{1}{12}bd^3$. As in the previous case, consider a crack of length a_p inside a pillar so that: $I_p = \frac{1}{12}b(d-a_p)^3$ and $A_p = b(d-a_p)$. Using Irwin-Kies equation, eq. (13), differentiating with respect to a_p results in:

$$\mathcal{G}_{sb} = 6\frac{P_{\tau}^2}{b^2} \frac{t^3}{E} (d - a_p)^{-4} + 2\frac{P_{\tau}^2 t}{\kappa G b^2} (d - a_p)^{-2}$$
(25)

which contains both the bending (the first term on the right hand side) and the shear part (second term) of the SERR. At the onset of the failure, i.e. $a_p \to 0$, we write:

$$\mathcal{G}_{sb} = \mathcal{G}_{csb} = 6\frac{P_{\tau}^2}{b^2} \frac{t^3}{E} d^{-4} + 2\frac{P_{\tau}^2 t}{\kappa G b^2} d^{-2}$$
(26)

Under the assumption $P_{\tau} = \tau bd$ yields bending:

$$\mathcal{G}_{cb} = 6\frac{\tau^2}{E} \frac{t^3}{d^2} \tag{27}$$

and shear:

$$\mathcal{G}_{cs} = 2\frac{\tau^2}{\kappa G}t\tag{28}$$

parts of the energy release rate. Interestingly, in ref. [2] within a slightly different context and using calculations including coarse grained atomistic simulations, the existence of a critical length scale parameter agreeing perfectly with t, which controls failure of friction adhesive junction, was discovered. Eqs. (23), (27) and (28) summarize the results of the micro-mechanical analysis and will serve as a basis for the experimental and numerical investigations.

4.2.3. Coupling Between Micro- and Macro-mechanical Models

A micro- and a macro-mechanical approach to describe the failure process of the configuration were developed in previous sections. In this section a coupling between them relating the macroscopic loading P to the resulting microscopic loading P_p and M_p is established. The pillars are assumed to act as linear springs with stiffness of the unit cell k. The traction, which acts on a pillar and is transferred to the beams, is equated as the extension of the pillar times the stiffness:

$$q(x) = k \cdot (w_t + w_b) \tag{29}$$

In the macro-mechanical configuration the single pillars are disregarded and a continuous, unit cell-based bondline is constructed. When shifting from the macroscopic to the microscopic configuration it is assumed that each pillar carries the loading of the corresponding unit cell. Furthermore, it is assumed that the overall failure of the structure is governed by the failure of the first pillar. Hence, the analysis is restricted to the first pillar only. The average stress acting on the first pillar is:

$$\sigma_p(x) = \frac{k}{(s+d)b} \int_a^{a+d+s} (w_t + w_b) dx$$
 (30)

Assuming that the adherend thickness remains unchanged, the local pillar extension can be found from the global deflection as:

$$w_t = w_2 (\beta = t)$$
 and $w_b = w_2 (\beta = b)$ (31)

When combining eqs. (30) and (31) the pillar stress becomes a function of the global loading P, hence, when inserted into eq. (23) a coupling between the macroscopic loading and the microscopic failure is realized.

5. Results and Discussion

5.1. Load Response

Fig. 5 shows representative force-displacement curves for: a) the reference specimen, and b) the symmetric DCB with a pillar interface. Both

specimens exhibit the same initial, linear loading up to crack onset, which is indicated by circular markers in the plots. For the reference specimens, Fig. 5(a), the initial linear loading path was replaced by another, almost linear, monotonically increasing in the present case. The deviation from the initial slope was caused by onset and propagation of the crack out from the initial plane defined by the pre-crack. In the experiments it was observed that the crack kinked out of the etched line and followed the shear band direction, resulting in catastrophic failure of the specimen.

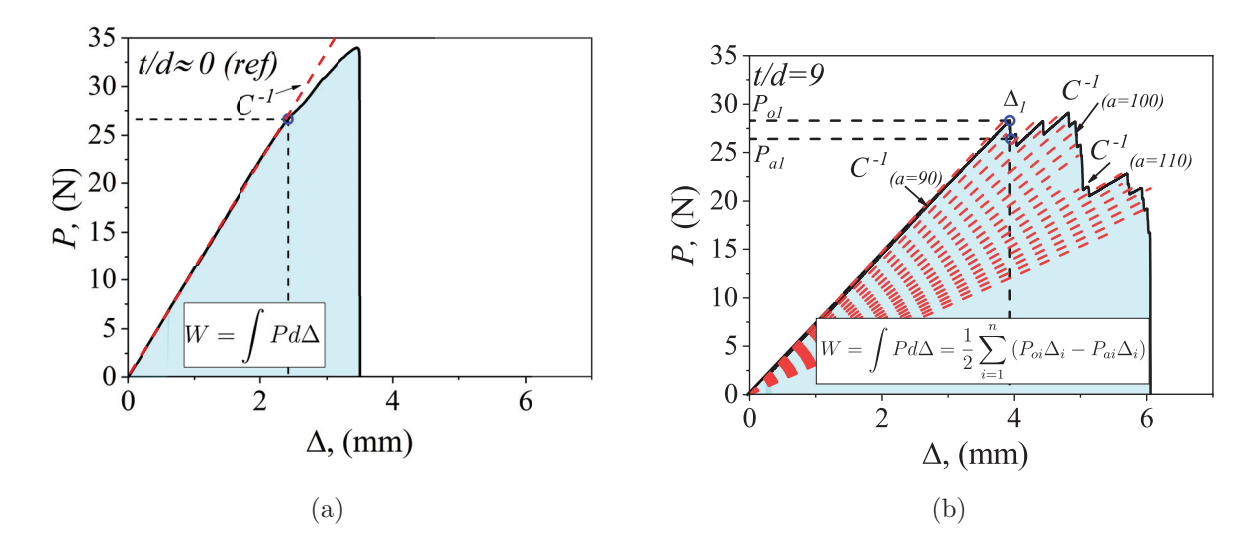


Figure 5: Experimental force-displacement curves. a) Reference specimen where the dashed, red line showing the initial linear, loading path. b) Asymmetric specimen with pillars of t/d=9. Red, dashed lines correspond to the compliance at specific crack lengths. The theoretical predictions agree very well with the positions of the pillars (2 mm separation). The cyan areas indicate the area use to evaluate the work of fracture - $W_{ref}=0.067\,\mathrm{J}$ and $W_{pillar}=0.106\,\mathrm{J}$.

A significantly different behavior is observed for the specimens with the

pillar interface. In Fig. 5(b) a representative curve for the symmetric specimen is seen (specimen with aspect ratio t/d=9). The initial loading persisted until the crack onset of the first pillar (marked by a circle). The failure of it led to a load drop (the second circle), however, load increased again after the crack reached the second pillar. Instead of catastrophic failure a new loading path is followed until the critical force for the next pillar is reached leading to its failure and a load drop, which is then recovered by the third pillar, and the process is repeated until the crack reached the last of the pillars. A non-steady state (effectively, the stick-slip) propagation is observed and is comprised of crack onsets and crack arrests. No kinking of the crack from the interface was observed in any of the experiments.

Together with the experimental data are depicted the theoretical loading paths (marked with dashed, red lines) obtained using eq. (12). Each loading path was calculated with an initial crack length corresponding to a well defined pillar position. For example, the first loading path corresponds to a crack length of $a_{lp1} = a_0 = 90 \,\mathrm{mm}$, the second path is calculated with $a_{lp2} = a_0 + (d+s) = 92 \,\mathrm{mm}$, and so on. The theoretical predictions of the loading paths correspond very well with those of the experimental data. This supports the idea of each pillar failing individually followed by crack arrest at the next pillar. Furthermore, this result shows that crack propagation is the main source of energy dissipation and it gives confidence that the use of the Irwin-Kies assumption [eq. (13)] is justified.

The crack propagation facilitated by multiple crack onsets and arrests gave the specimen a much larger extension range and associated work done i.e. $W = \int P d\Delta = \frac{1}{2} \sum_{i=1}^{n} \left(P_{oi} \Delta_i - P_{ai} \Delta_i \right) \propto n$ where $W, P_{oi}, P_{ai}, \Delta_i, n$

denote the work done by structured interface, force at crack onset in pillar i, force at crack arrest position of pillar i, displacement at pillar i and the number of pillars, respectively, compared to the kinking crack, which in the present study always led to critical failure soon after onset.

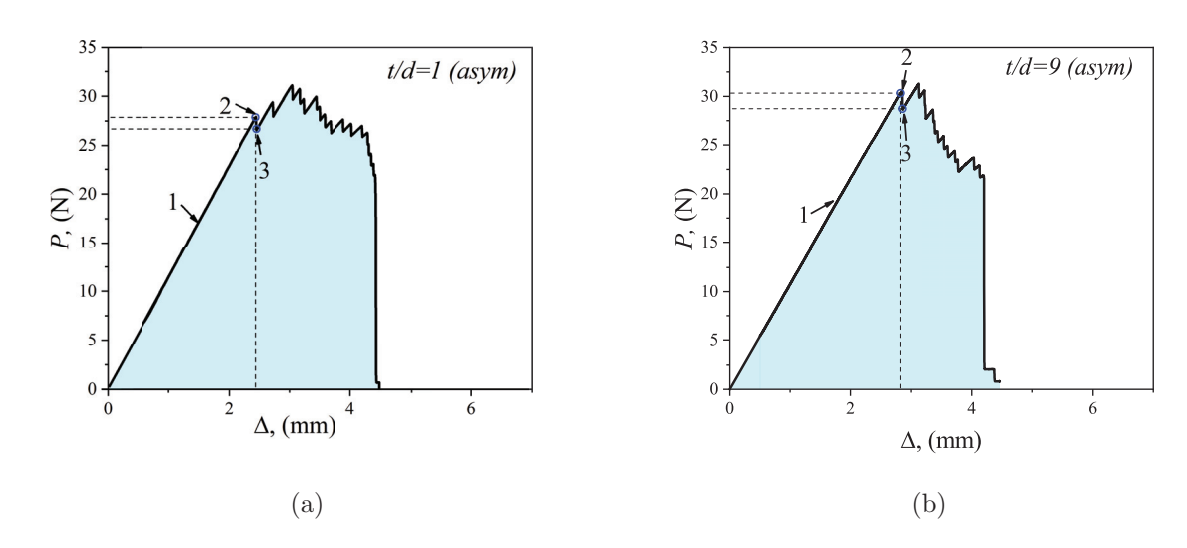


Figure 6: Experimental force-displacement curves. a) Asymmetric DCB with a top adherend 1.5 times thicker than the bottom adherend. The pillars had an aspect ratio of t/d=1. b) Asymmetric DCB with pillars of aspect ratio t/d=9. The different marks indicate 1) initial loading path, 2) crack onset / loss of linearity, 3) point of crack arrest and beginning of new loading path. The cyan areas depict the work of $W_{t/d=1}=0.090\,\mathrm{J}$ and $W_{t/d=9}=0.080\,\mathrm{J}$

For comparison, Fig. 6(a) and (b) show the exemplary load response for asymmetric specimens with the pillars of aspect ratios of t/d = 1 and t/d = 9, respectively. The same main features of the force-displacement curves are revealed viz. crack onset-arrest behavior visible from the characteristic jagged form (in Fig. 6 the numbers 1-3 denotes linear loading, crack

onset and crack arrest stages respectively). It is noticed that introducing asymmetry to the configuration did not affect the load response significantly. Comparing the responses for different pillar heights, they are very similar in terms of qualitative behavior.

5.1.1. Compliance

Figure 7 shows the compliance (normalized by the theoretical compliance of the reference geometry) as a function of the aspect ratio of the pillars obtained from the experiments, the analytical prediction in eq. (12), and from the FEA. The three approaches can be found in very good agreement. As anticipated, the thicker substrate (higher bending and shear rigidities) shifted the compliance to a lower state not affecting the overall trend of the curve. The compliance was expected to increase with increasing pillar aspect ratio as indicated by eq. (3). This is also seen in Fig. 7. Both the analytical model and the FEA predict the compliances for both configuration in the tested range of pillar aspect ratios. However, the analytical model for the asymmetric configuration slightly underestimates the compliance of the specimen. It should be noticed that for the limiting case, where the aspect ratio tends toward zero the analytical model converges to the reference model. For a pillar aspect ratio of t/d = 9, the compliance is around 13 % higher than for the reference DCB specimen. The good agreement between the FEA, which accounted for the structure of each pillars, and the analytical model, which homogenized the pillars and interface, supports the assumptions made for the latter.

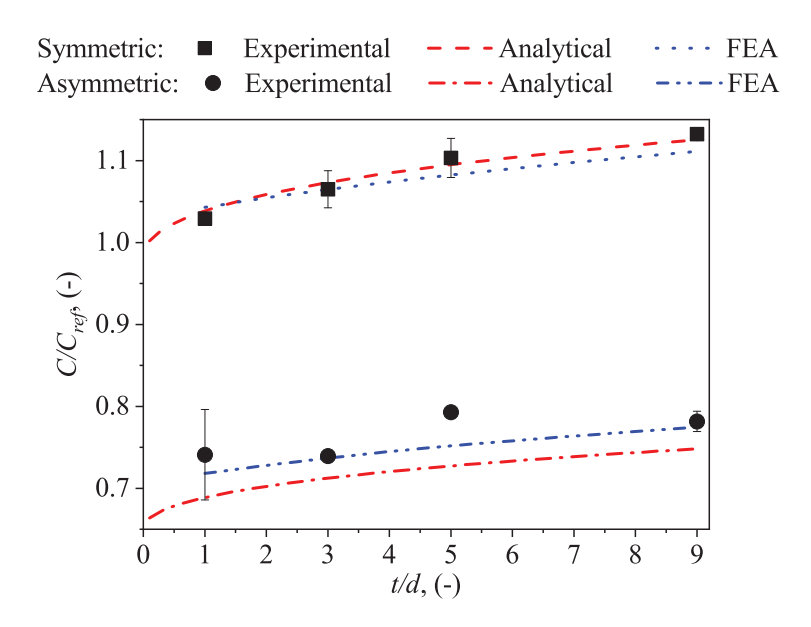


Figure 7: Specimen compliance normalized with the theoretical reference geometry against aspect ratio of the interfacial pillars. The squares and circles show the mean values and accompanying standard deviations of the experimental compliances from the symmetric and asymmetric configuration, respectively. The red lines (dashed for symmetric and dashed-dotted for asymmetric) are the analytical model showing a very good agreement with the experimental data. The asymmetric configuration is slightly overestimated in terms of stiffness. The symmetrical configuration converges to the reference model in the limiting case where $t/d \to 0$. The FEA, depicted with blue lines (dotted for symmetric and dashed-dotted-dotted for asymmetric), also shows a very good agreement with both the analytical model and the experimental data.

5.1.2. Finite Element Analysis of Load Transfer

In Fig. 8(a-d) the normal stress, σ_{yy} , along the centreline of the interface region (as depicted in Fig. 3) of symmetric specimens with four different aspect ratios are shown. All of the four cases are presented as per unit of applied force.

The red and blue regions depict the axial stress (tension and compression, respectively) in the pillars. For the lowest of the aspect ratios the stress distribution takes on a parabolic shape with largest magnitude in the middle of the pillar. This specific shape is due to the finite height of the pillar for which the center, y = 0, remains affected by the corner stress effects at y = t/2. The overall stress distribution resembles the shape predicted by the homogenized version of the elastic foundation model [eq. (7)] plotted as a continuous black line. The peak stress, at the first pillar, i.e. governing failure load, is found to decrease significantly with increasing pillar aspect ratio. Increasing the aspect ratio from t/d = 1 to t/d = 10 reduces the peak stress on the first pillar by half.

A red, dashed line tracing the upper envelope of the stress in each pillar for the aspect ratio t/d=1 in the first Fig. 8(a). The same dashed line is then plotted in the three, subsequent figures to visualize the effect of the pillar aspect ratio on the stress. This reveals an interesting trend where the stress in the first few pillars decrease as the aspect ratio goes up while more and more pillars are affected. Hence, larger aspect ratios prompt better stress distribution with the stress spread across more pillars. The distance from the crack tip to the end of the tensile zone (the process zone length) as obtained from the FE calculations is shown on the graphs as λ_{fe}^{-1} . This characteristic

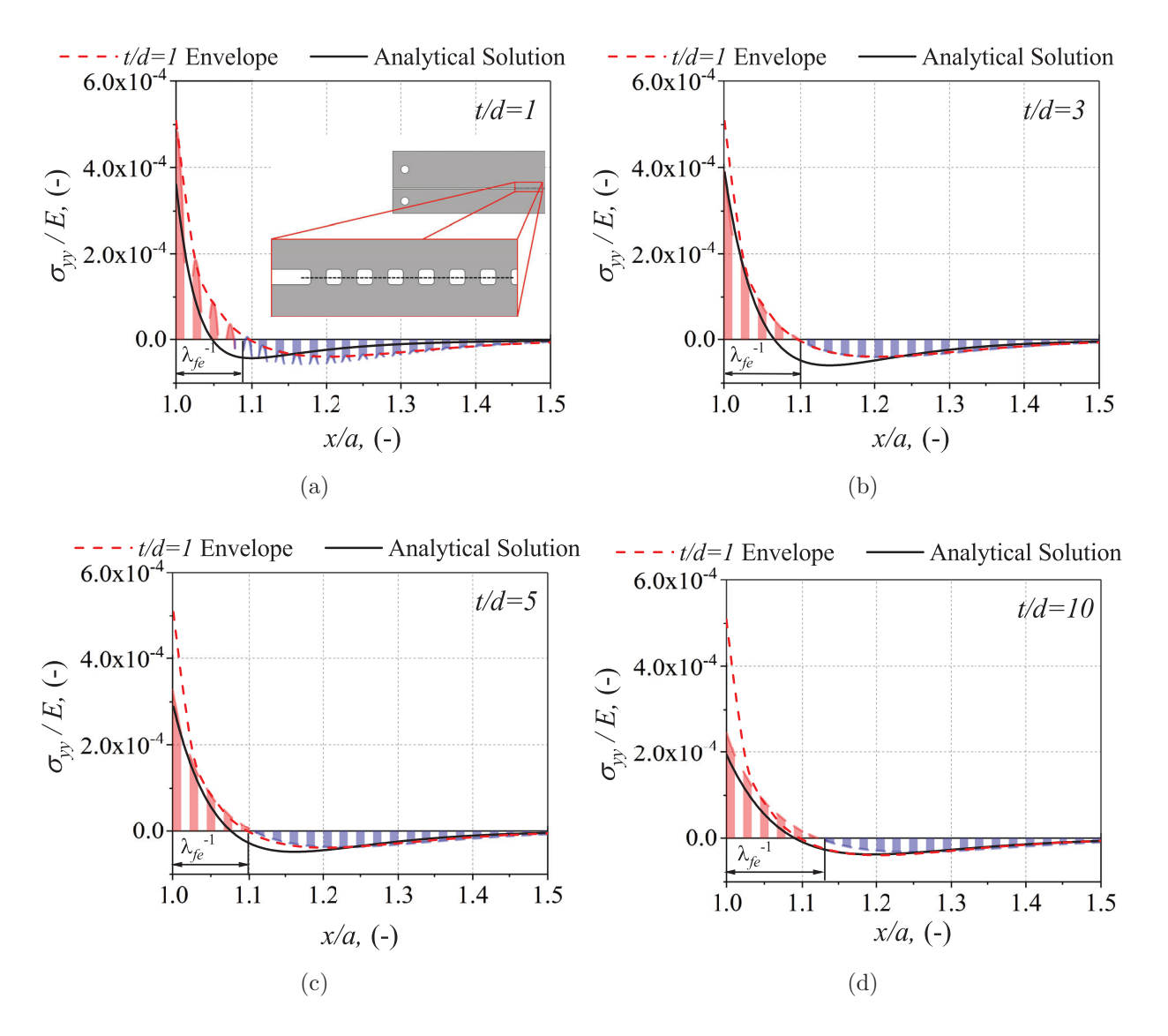


Figure 8: FEA predictions of the stress σ_{yy} distribution in the pillars for the symmetric configuration. The red and blue regions depict the axial stress (tension and compression, respectively) in the pillars. The dashed, red lines show the upper envelope of the pillars with aspect ratios t/d=1. The process zone λ_{fe}^{-1} spanning from the crack tip to the beginning of the compression zone is marked as well. The black lines show the analytical solution given by eq. (7).

length increases by 1.5 times between t/d = 1 and t/d = 10 cases, resulting in two additional pillars carrying the load in the t/d = 10. This is in agreement with eq. (9), which reveals that the elastic process zone increases with the aspect ratio of pillars. The failure of the specimen is assumed to be governed by the failure of the first pillar and the peak stress in it decreases with increasing aspect ratios, thus slender pillars should promote larger critical failure loads. Moreover, the product of $\lambda^{-1}\lambda_{fe} \to 1$ as $\frac{t}{d} \to \infty$, which indicates that the homogenized model may form a reference, asymptotic, solution. However, we expect the other non-dimensional interface parameter s/d to play an important role, which suggests a possible extension of the present work.

Let us briefly discuss consequences of the load distribution on the crack growth process by starting out with the unloaded configuration: $P = \Delta = 0$ in Fig. 5. Upon load application the stresses along the interface are distributed along λ^{-1} and the number of load sharing pillars is established. The stress level on the first pillar is below the critical value (recognized as critical force P_c). Once the critical stress on the first pillar is reached, the pillar breaks instantaneously. As reported for the homogeneous geometry (Appendix A1), due to the brittleness of the material and the finite (and small) width of the pillar, stable crack growth cannot be expected. The energy is released and the crack front position moves to the next pillar (i.e. $a_0 \rightarrow a_0 + d + s$). The process zone is re-established with the same number of pillars carrying the load as before, but the peak stress value (for the displacement controlled boundary conditions) is below the critical. Additional energy needs to be supplied to overcome the threshold value and propagate

the crack further. The entire process is iterative as seen from Figs. 5 and 6. Due to the finite size of the pillars and the distance between them, the process is dominated by deterministic effects and can be related to lattice fracture models [31]. However, by increasing the number of pillars in the width direction or by reducing the gap s between the pillars, such that the stresses shared by two neighboring pillars will be of similar magnitude [13], it can turn into a more stochastic process. Further analysis of such transition is beyond the scope of the present study.

To complete this section, in Fig. 9 the axial stress in the pillars for the asymmetric configurations are shown. The asymmetric specimen has a very similar trend to the symmetric specimen for both the stress distribution across a single pillar and the overall distribution across the interface. Both configurations stays in good agreement qualitatively and quantitatively, hence asymmetry, in the present case, does not seem to significantly affect the long-range distribution of the tensile component of the stress.

The asymmetric configuration results in additional shearing of the interface. In Fig. 10 the shear stress σ_{xy} distribution is shown. Common for all aspect ratios is that the shearing is largest in the middle of the pillars while it is zero near the edges (shear stress free). Like the axial stresses, the shear stresses decrease with increasing aspect ratio, however, the shear stresses are an order of magnitude smaller than the axial stresses. Recall, that peak axial stress decreased by a factor of 2 when the aspect ratio went from t/d = 1 to t/d = 10. The peak shear stress decreases by almost a factor of 30 for the same aspect ratio range. As expected from the macro-mechanical model, eq. (26), the increased aspect ratio allows accommodation of the effects of

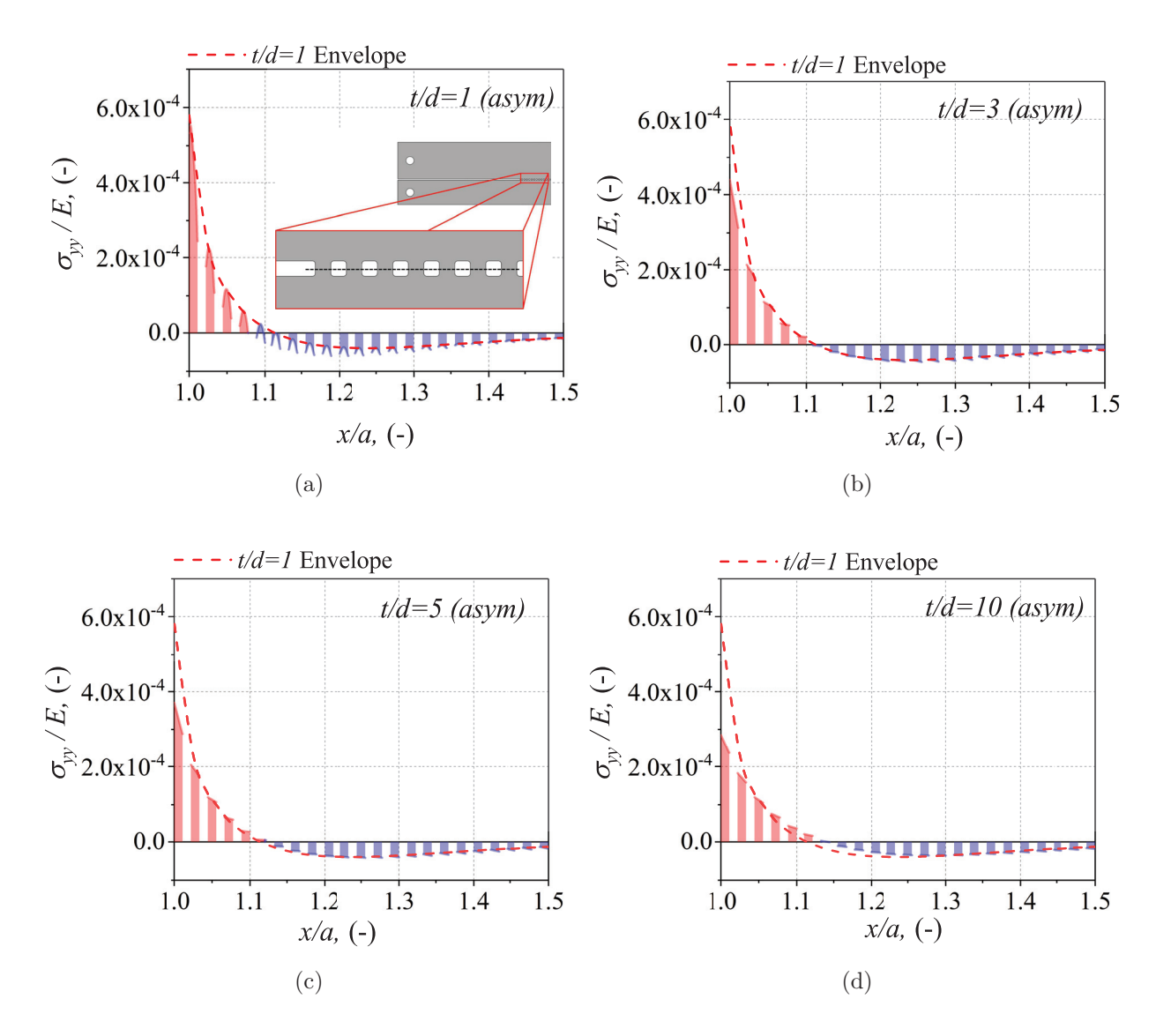


Figure 9: FEA predictions of the distribution of axial stress σ_{yy} in the pillars for the asymmetric configuration. The red and blue pillars depict the tension and compression, respectively, in the pillars. The dashed, red lines are the upper envelope of the pillars with aspect ratio t/d=1.

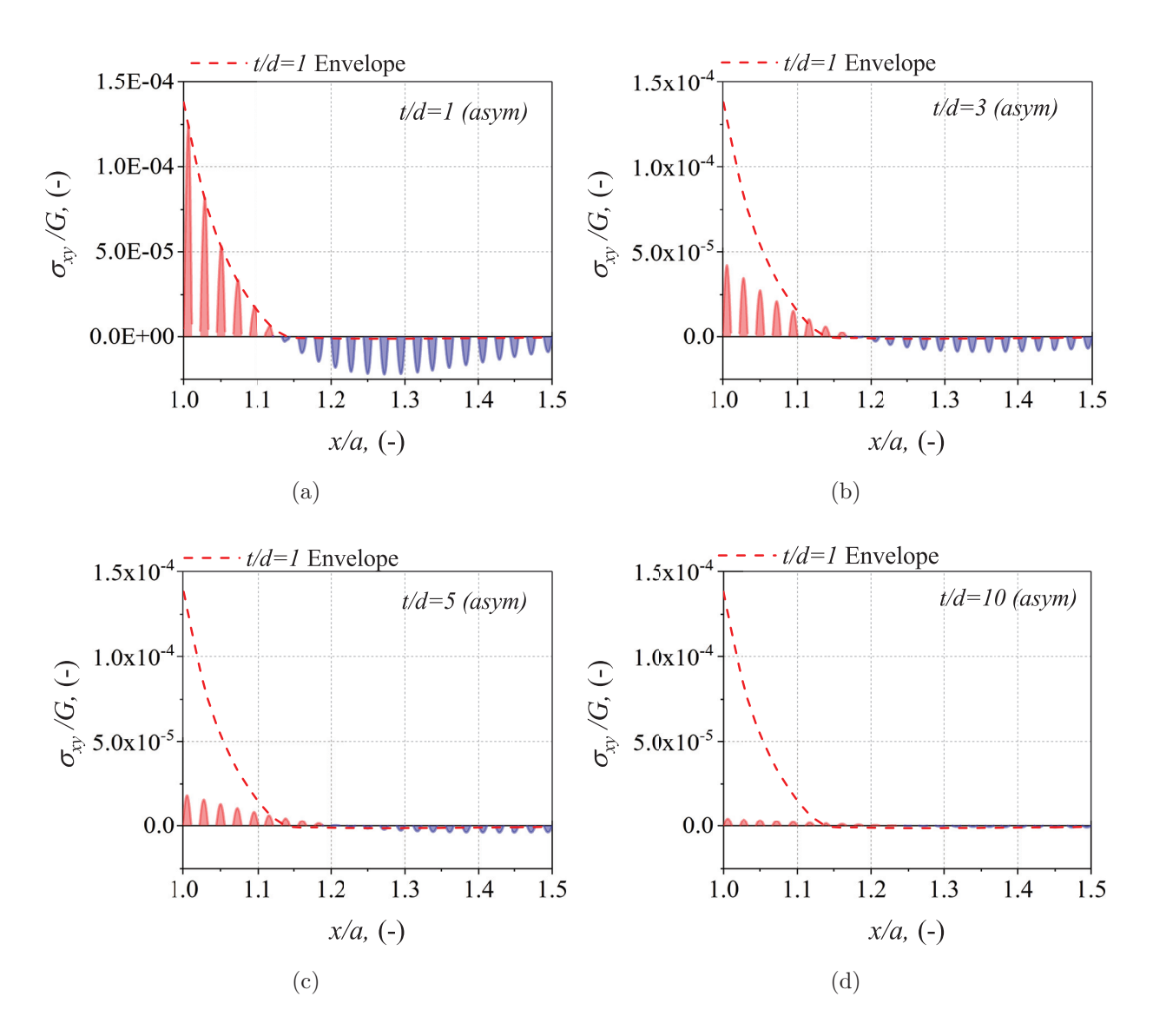


Figure 10: Shear stress across the pillars in the asymmetric configuration. The red and blue pillars show the positive and negative shear stresses, respectively, obtained from FEA normalized with the shear modulus G. The dashed, red line is the upper envelope of the t/d=1 specimen.

specimen asymmetry, turning the shear dominated, stubby, geometry of the pillars (t/d < 1) to a more slender one (t/d > 1) in which bending prevails. While, in the present study the axial loading of the pillars is dominant and the shear stresses can be neglected from here on, the work also encourages further investigation of t/d < 1 cases under mixed mode conditions.

5.2. Micro-mechanics vs. Macro-mechanics

In the following, the difference between the macroscopic and the microscopic approaches is described including the relation to the experimental observations.

5.2.1. Critical Fracture Force

As mentioned before, variations in the critical force, i.e. the force at crack onset, were determined for different specimen types and different pillar aspect ratios. The critical force for the symmetric and asymmetric specimens are shown by squares and circles, respectively, in Fig. 11. For comparison the critical forces are normalized with that of the reference specimens, $P_{c,ref}$. The results show that the onset force P_c decreases by around 20% relative to the reference specimen for aspect ratios up to t/d = 1. However, the critical force monotonically increases with increasing aspect ratios once t/d > 1. This supports the idea from the previous section of slender pillars aiding the stress distribution.

Recall, that within the present study the reference specimen broke abruptly, while the pillared specimen promoted crack propagation with multiple onsets and arrests. Introducing pillars at the interface increased work of fracture at the cost of a slightly lower onset force compared to the reference geometry, at

least for the aspect ratios treated in this work. The trend of the data predicts that at certain aspect ratios t/d > 9 the critical force could be similar, even higher, than for the reference configuration. This observation suggests using fibril geometries $t/d \gg 1$, in agreement with the load sharing phenomena observed in fibrillar adhesives [7, 27, 3].

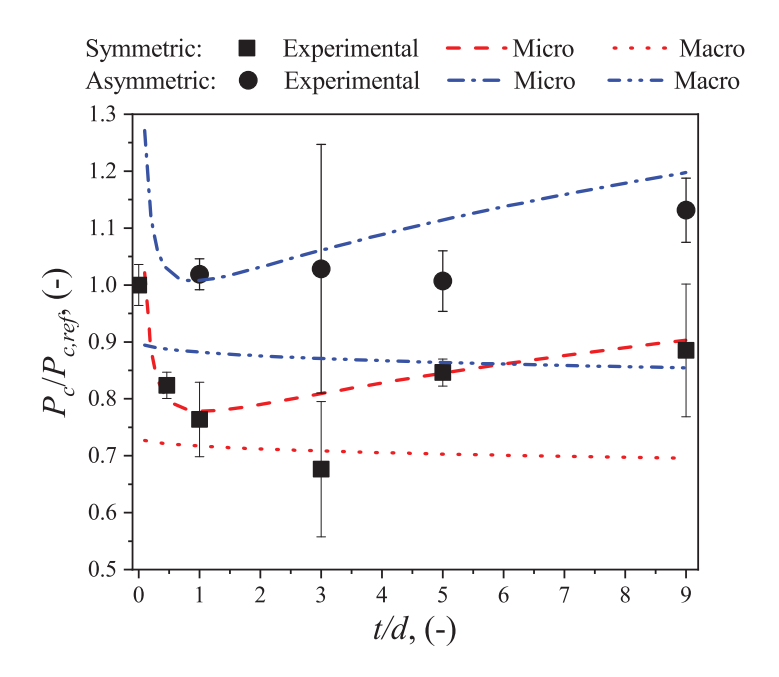


Figure 11: Critical onset force normalized by the onset force of the reference specimen as function of the pillar aspect ratio. The squares and the circles show the experimental mean critical force and standard deviation for the symmetric and asymmetric configuration, respectively. The dotted and dashed-dotted-dotted lines show the predictions of the macro-mechanical approach and the dashed and dashed-dotted lines represent the micro-mechanical approach with red and blue lines for the symmetric and asymmetric configuration, respectively. Increasing critical force with increasing aspect ratio is observed. This was captured by the micro-mechanical approach while the macroscale approach fails to capture this trend.

In Fig. 11 the predictions of the micro-mechanical and the macro-mechanical approaches are shown with dashed and dashed-dotted, and, dotted and dashed-dotted-dotted lines, respectively, with red color used for the symmetric and blue for the asymmetric specimens. Recall, that the macroscopic approach was based on the Irwin-Kies equation, eq. (38), and the formulation treating the interface as homogeneous and continuous. The microscopic approach, eq. (23), was based on an energetic analysis of the pillar taking its geometry into account. Importantly, even though the macro-mechanical model successfully captured the compliance of the configurations it failed to predict the critical force accurately. It underestimates the onset force while predicting a decreasing trend with increasing aspect ratio - the opposite of what is observed. The micro-mechanical approach, however, is in very good agreement with the experimental data both qualitatively and quantitatively. This supports the concept of failure being governed by the micro-mechanical mechanisms and, thus, the macroscopic approach alone is insufficient.

Importantly, the macroscopic response of the material to applied load can be fully controlled through smaller scale geometrical manipulations being the core of mechanical metamaterials.

5.3. Interface Material Failure Scaling Law

The scaling law derived in [8] suggests that the critical force of a bonded system is governed by the fracture energy \mathcal{G}_c , the contact area A, and, the compliance of the system C, i.e.:

$$P_c \sim \sqrt{\mathcal{G}_c} \sqrt{\frac{A}{C}}$$
 (32)

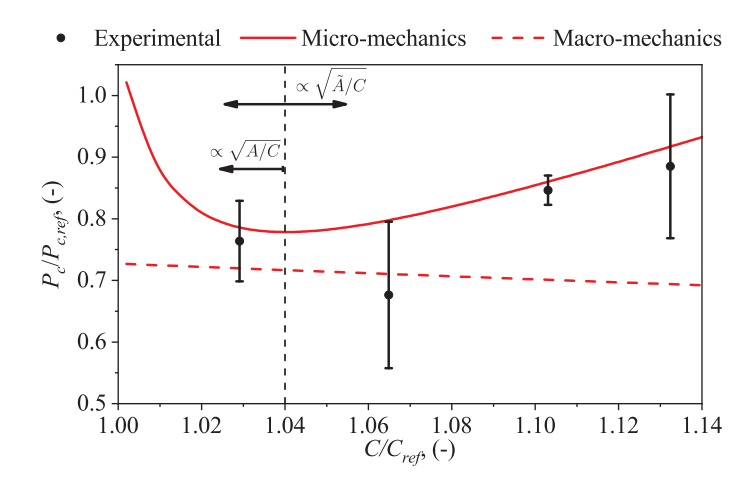


Figure 12: Relation between the compliance and the critical force for the symmetric configuration. The global approach (dashed line) follows an inversely proportional relation that agrees with the scaling law proposed by [8] when the surface area is kept constant. The experimental (circles) and the micro-mechanical approach (solid line), however, show proportionality between the critical force and the compliance.

In the present work, the area created during a single failure event is $b \cdot d = \text{const.}$ However, Fig. 7 indicates that the compliance increased with the aspect ratio d/t such that the ratio $R_{AC} := \sqrt{A/C} \to 0$ as $t/d \to \infty$. Thus, the critical force was expected to decrease.

5.3.1. The Effective Load Carrying Area

In Fig. 12 the macro-mechanical and micro-mechanical approaches depict the relation between the normalized critical force and the compliance. The data are compared with experimental results. Both, the micro-mechanical approach and the experimental data display similar trend. Except at the very beginning, the critical force increased with increasing compliance, thereby contradicting the scaling in eq. (32). Assuming that the region responsible for load transfer ahead of the crack front is related to the elastic process zone of length λ^{-1} , the affected area can be defined by combining eqs. (3) and (9):

$$\tilde{A} := \lambda^{-1} b f = \left(2 I_{\beta} b^{3}\right)^{1/4} \left[\frac{d^{4}}{(d+s)^{3}}\right]^{1/4} \left(\frac{t}{d}\right)^{1/4}$$
(33)

The first term on the right-hand side represents the effect of the geometry of the substrates defining the 'long range interactions' length scale of the material. The second term expresses the characteristic, in-plane structure of the interface and is responsible for the efficiency of the load transfer between the long and short ranges. The third term reflects the smallest geometrical feature of the material, which in the present case is the pillar aspect ratio. Increasing either the dimensions of the substrate, the volume fraction of the pillars, or the pillar aspect ratio increases the load carrying area by extending the process zone. Since the compliance, eq. (12), is proportional to the aspect ratio, the ratio $\sqrt{A/C}$ also decreases with the aspect ratio when the area is fixed.

5.3.2. The Surface Area-Compliance Ratio

If the area increases, it is the competition between the growth of the area and that of the compliance, which determines if the ratio and, hereby, the critical force increases or decreases. The ratios R_{AC} for the experimental data and the analytical model are obtained using eq. (32), the critical force and the fracture energy, hence:

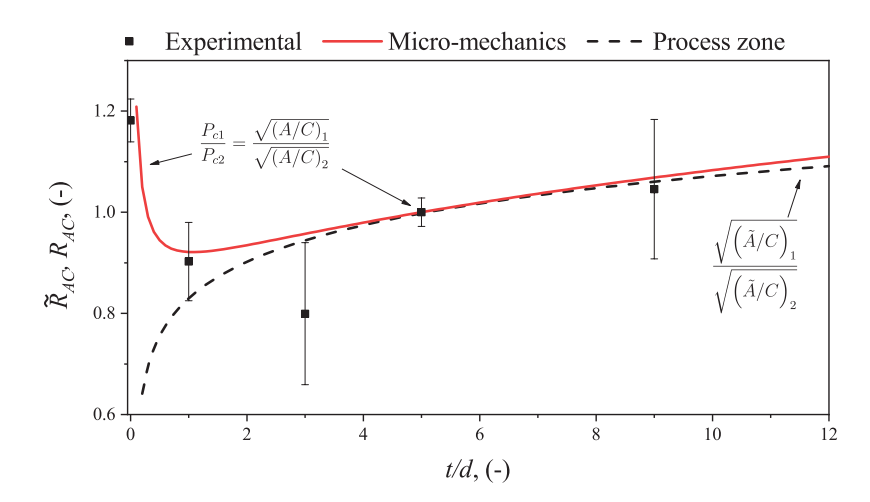


Figure 13: Relation between the pillar aspect ratio t/d and normalized the surface areacompliance ratios \tilde{R}_{AC} and R_{AC} . The dashed line shows the relation when only the load carrying surface area as stated in eq. (33) is taken into account. The solid line represents the micro-mechanical model and the squares depict the experimental data. Both of them are calculated based on the scaling law eq. (32) using the critical forces. An acceptable agreement between the different approaches and the experimental data is seen, especially for higher aspect ratios.

$$R_{AC} := \frac{R_{AC1}}{R_{AC2}} = \frac{P_{c1}}{P_{c2}} = \frac{\sqrt{\mathcal{G}_c} \left(\sqrt{\frac{A}{C}}\right)_1}{\sqrt{\mathcal{G}_c} \left(\sqrt{\frac{A}{C}}\right)_2}$$
(34)

referred to as the 'force approach'. For comparison, a similar normalization is applied to $\tilde{R}_{AC}=\sqrt{\tilde{A}/C}$, referred to as the 'affected area' approach. In both cases t/d = 5 is used as reference (regarded as intermediate case). In Fig. 13 the three ratios are shown as functions of the pillar aspect ratio. A good agreement between the different approaches and the experimental data is observed. However, in the limit $\frac{t}{d} \to 0$, the interface region geometry translates to (flat) spots and both approaches diverge rapidly. Quantitatively minor discrepancies are revealed between the critical force approach and the affected area approach while qualitative resemblance is good. The dashed line representing the affected area approach increases with the aspect ratio, which means that the affected area grows faster than the compliance of the system. Both methods stay in good agreement with the experimental data. This indicates that the critical force scales with the load carrying interface area ahead of the crack, as stated by eq. (33), and not the surface area of the pillar alone. This has two implications. Firstly, the scaling law is still valid for this configuration, however, instead of the geometrical interface area A, the load carrying area \tilde{A} should be included:

$$P_c \sim \sqrt{\mathcal{G}_c} \sqrt{\frac{\tilde{A}}{C}} \tag{35}$$

Secondly, the critical force can be tuned without changing the geometrical interface area as shown in this study. From eq. (33) it is seen that both the geometry, the composition of pillars and their spacing, and, the pillar aspect ratio influence the affected surface area and through it the critical force. This provides a powerful tool for understanding and designing materials with structured interfaces since these terms also affect the overall compliance allowing for tougher and more compliant structures.

6. Conclusions

We have investigated the use of geometry to engineer the fracture response of double cantilever beam specimens. Double cantilever beam reference specimens were laser cut from thin sheets of elastic-brittle PMMA and tested under mode I loading. Unstable crack growth and rapid catastrophic failure due to crack kinking were recorded in unstructured specimens. The introduction of geometrical features in the form of an array of pillars significantly altered the fracture response of the specimen. Thus, a new "material" is produced with properties depending on the intertwined length scales introduced by 'long range' beam and 'short range' pillar geometries. This led to a significant alteration of the load response of both quantitative and qualitative nature. The pillars caused a change from the single loading-critical failure event to a multiple failure event postponing the catastrophic failure, thus, significantly increasing the energy dissipated in fracture of the specimens. For displacement-controlled experiments multiple failure events are guaranteed and independent of the pillar geometry. Importantly, the model provided can be used for designing interfaces maintaining such behavior under force controlled (unstable) loading. This can be achieved through the indicated parameters: thickness and width of the pillar, distance between the pillars, and the process zone size. The compliance and the critical fracture load were found to be affected by the geometrical features as well. Specifically, the compliance and failure load both increased with increasing pillar aspect ratio. Moreover we noted that the structured pillar interface, i.e. the micro-scale in our problem, were capable of absorbing a certain degree of imperfection, e.g. asymmetry. This provides a tool for increasing energy dissipation through interfaces but also for tuning structural properties.

While in this work the simplest geometrical modifications have been made, the observed phenomena and gains displayed a significant potential for geometric manipulation to achieve tougher or tuned properties.

Acknowledgments

Financial support from IDAs og Berg-Nielsens Studie- og Støttefond, Aage og Johanne Louis-Hansens Fond, Augustinus Fonden and Knud Højgaards Fond are gratefully acknowledged. KTT acknowledges financial support for this work from the National Science Foundation under awards CMMI-1663037 and MRSEC DMR-1720530.

References

- [1] Abid, N., Pro, J. W., Barthelat, F., 2019. Fracture mechanics of nacrelike materials using discrete-element models: Effects of microstructure, interfaces and randomness. Journal of the Mechanics and Physics of Solids 124, 350–365.
- [2] Aghababaei, R., Warner, D. H., Molinari, J.-F., sep 2016. Critical length scale controls adhesive wear mechanisms. Nature Communications 7 (1), 11816.
- [3] Aksak, B., Murphy, M. P., Sitti, M., may 2008. Gecko inspired microfibrillar adhesives for wall climbing robots on micro/nanoscale rough surfaces. In: 2008 IEEE International Conference on Robotics and Automation. IEEE, pp. 3058–3063.
- [4] Ashby, M., Johnson, K., 2010. Materials and Design, 2nd Edition. Butterworth-Heinemann, Canada.
- [5] Autumn, K., Gravish, N., 2008. Gecko adhesion: Evolutionary nanotechnology. Philosophical Transactions of the Royal Society A: Mathematical, Physical and Engineering Sciences 366 (1870), 1575–1590.
- [6] Ayatollahi, M. R., Aliha, M. R., Hassani, M. M., 2006. Mixed mode brittle fracture in PMMA - An experimental study using SCB specimens. Materials Science and Engineering A 417 (1-2), 348–356.
- [7] Bacca, M., Booth, J. A., Turner, K. L., McMeeking, R. M., 2016. Load sharing in bioinspired fibrillar adhesives with backing layer interactions

- and interfacial misalignment. Journal of the Mechanics and Physics of Solids 96, 428–444.
- [8] Bartlett, M. D., Croll, A. B., King, D. R., Paret, B. M., Irschick, D. J., Crosby, A. J., 2012. Looking beyond fibrillar features to scale gecko-like adhesion. Advanced Materials 24 (8), 1078–1083.
- [9] Bažant, Z. P., Cedolin, L., 2010. Stability of structures: Elastic, inelastic, fracture and damage theories. Stability of Structures: Elastic, Inelastic, Fracture and Damage Theories, 1–1012.
- [10] Bertoldi, K., Vitelli, V., Christensen, J., van Hecke, M., nov 2017. Flexible mechanical metamaterials. Nature Reviews Materials 2 (11), 17066.
- [11] Bonesteel, R. M., Piper, D. E., Davinroy, A. T., 1978. Compliance and KI calibration of double cantilever beam (DCB) specimens. Engineering Fracture Mechanics 10 (2), 425–428.
- [12] Chaudhury, M. K., Chakrabarti, A., Ghatak, A., jul 2015. Adhesion-induced instabilities and pattern formation in thin films of elastomers and gels. The European Physical Journal E 38 (7), 82.
- [13] Chung, J. Y., Chaudhury, M. K., 2005. Roles of discontinuities in bioinspired adhesive pads. Journal of the Royal Society Interface 2 (2), 55–61.
- [14] Deblieck, R. A., Van Beek, D. J., Remerie, K., Ward, I. M., 2011. Failure mechanisms in polyolefines: The role of crazing, shear yielding and the entanglement network. Polymer 52 (14), 2979–2990.

- [15] Del Campo, A., Greiner, C., Arzt, E., 2007. Contact shape controls adhesion of bioinspired fibrillar surfaces. Langmuir 23 (20), 10235–10243.
- [16] Dillard, D. A., Mukherjee, B., Karnal, P., Batra, R. C., Frechette, J., 2018. A review of Winkler's foundation and its profound influence on adhesion and soft matter applications. Soft Matter 14 (19), 3669–3683.
- [17] Geim, A. K., Dubonos, S. V., Grigorieva, I. V., Novoselov, K. S., Zhukov, A. A., Shapoval, S. Y., jul 2003. Microfabricated adhesive mimicking gecko foot-hair. Nature Materials 2 (7), 461–463.
- [18] Glassmaker, N. J., Jagota, A., Hui, C. Y., Noderer, W. L., Chaudhury, M. K., 2007. Biologically inspired crack trapping for enhanced adhesion. Proceedings of the National Academy of Sciences of the United States of America 104 (26), 10786–10791.
- [19] Gómez, F. J., Elices, M., Valiente, A., 2000. Cracking in PMMA containing U-shaped notches. Fatigue and Fracture of Engineering Materials and Structures 23 (9), 795–803.
- [20] Griffith; A., Eng, M., 1920. VI. The phenomena of rupture and flow in solids. Philosophical Transactions of the Royal Society of London. Series A, Containing Papers of a Mathematical or Physical Character.
- [21] Grossman, M., Pivovarov, D., Bouville, F., Dransfeld, C., Masania, K., Studart, A. R., 2019. Hierarchical Toughening of Nacre-Like Composites. Advanced Functional Materials 29 (9).

- [22] Heide-Jørgensen, S., Budzik, M. K., 2017. Crack growth along heterogeneous interface during the DCB experiment. International Journal of Solids and Structures 120, 278–291.
- [23] Heide-Jørgensen, S., Budzik, M. K., 2018. Effects of bondline discontinuity during growth of interface cracks including stability and kinetic considerations. Journal of the Mechanics and Physics of Solids 117, 1–21.
- [24] Heide-Jørgensen, S., Møller, R. K., Buhl, K. B., Pedersen, S. U., Daasbjerg, K., Hinge, M., Budzik, M. K., 2018. Efficient bonding of ethylene-propylene-diene M-class rubber to stainless steel using polymer brushes as a nanoscale adhesive. International Journal of Adhesion and Adhesives 87, 31–41.
- [25] Heide-Jørgensen, S., Teixeira de Freitas, S., Budzik, M. K., 2018. On the fracture behaviour of CFRP bonded joints under mode I loading: Effect of supporting carrier and interface contamination. Composites Science and Technology 160, 97–110.
- [26] Huang, Z., Li, X., dec 2013. Origin of flaw-tolerance in nacre. Scientific Reports 3 (1), 1693.
- [27] Hui, C. Y., Glassmaker, N. J., Tang, T., Jagota, A., 2004. Design of biomimetic fibrillar interfaces: 2. Mechanics of enhanced adhesion. Journal of the Royal Society Interface 1 (1), 35–48.
- [28] Hutchinson, R. G., Fleck, N. A., 2005. Microarchitectured cellular solids
 The hunt for statically determinate periodic trusses. ZAMM Zeitschrift
 fur Angewandte Mathematik und Mechanik 85 (9), 607–617.

- [29] Hutchinson, R. G., Fleck, N. A., 2006. The structural performance of the periodic truss. Journal of the Mechanics and Physics of Solids 54 (4), 756–782.
- [30] Irwin, G., 1957. Analysis of Stresses and Strains Near the End of a Crack Traversing a Plate.
- [31] Lawn, B., 1993. Fracture of brittle solids. Cambridge University Press, Cambridge.
- [32] Maloney, K., Fleck, N., 2018. Damage tolerance of an architected adhesive joint. International Journal of Solids and Structures 132-133, 9–19.
- [33] Maloney, K., Fleck, N., 2019. Toughening strategies in adhesive joints. International Journal of Solids and Structures 158, 66–75.
- [34] Messner, M. C., 2016. Optimal lattice-structured materials. Journal of the Mechanics and Physics of Solids 96, 162–183.
- [35] Minsky, H. K., Turner, K. T., 2017. Composite Microposts with High Dry Adhesion Strength. ACS Applied Materials and Interfaces 9 (21), 18322–18327.
- [36] Mojdehi, A. R., Holmes, D. P., Dillard, D. A., 2017. Revisiting the generalized scaling law for adhesion: Role of compliance and extension to progressive failure. Soft Matter 13 (41), 7529–7536.
- [37] Murphy, M. P., Aksak, B., Sitti, M., feb 2009. Gecko-inspired directional and controllable adhesion. Small 5 (2), 170–175.

- [38] Neggers, J., Hoefnagels, J. P., Van Der Sluis, O., Geers, M. G., 2015. Multi-scale experimental analysis of rate dependent metal-elastomer interface mechanics. Journal of the Mechanics and Physics of Solids 80, 26–36.
- [39] Ortiz, C., Boyce, M. C., feb 2008. Bioinspired Structural Materials. Science 319 (5866), 1053–1054.
- [40] Ostoja-Starzewski, M., jan 2002. Lattice models in micromechanics. Applied Mechanics Reviews 55 (1), 35–60.
- [41] Paris, P., Sih, G., 2009. Stress Analysis of Cracks. In: Fracture Toughness Testing and its Applications. ASTM International, 100 Barr Harbor Drive, PO Box C700, West Conshohocken, PA 19428-2959, pp. 30–30–52.
- [42] Rayneau-Kirkhope, D., Dias, M. A., aug 2017. Embracing failure. Physics World 30 (8), 25–28.
- [43] Salem, N. B., Budzik, M. K., Jumel, J., Shanahan, M. E., Lavelle, F., 2013. Investigation of the crack front process zone in the double cantilever beam test with backface strain monitoring technique. Engineering Fracture Mechanics 98 (1), 272–283.
- [44] Wadley, H. N., Fleck, N. A., Evans, A. G., 2003. Fabrication and structural performance of periodic cellular metal sandwich structures. Composites Science and Technology 63 (16), 2331–2343.
- [45] Walia, S., Shah, C. M., Gutruf, P., Nili, H., Chowdhury, D. R., Withayachumnankul, W., Bhaskaran, M., Sriram, S., mar 2015. Flexible meta-

- surfaces and metamaterials: A review of materials and fabrication processes at micro- and nano-scales. Applied Physics Reviews 2 (1), 011303.
- [46] Wegst, U. G., Bai, H., Saiz, E., Tomsia, A. P., Ritchie, R. O., 2015.
 Bioinspired structural materials. Nature Materials 14 (1), 23–36.
- [47] Xue, L., Sanz, B., Luo, A., Turner, K. T., Wang, X., Tan, D., Zhang, R., Du, H., Steinhart, M., Mijangos, C., Guttmann, M., Kappl, M., Del Campo, A., 2017. Hybrid Surface Patterns Mimicking the Design of the Adhesive Toe Pad of Tree Frog. ACS Nano 11 (10), 9711–9719.
- [48] Yang, Y., Dias, M. A., Holmes, D. P., nov 2018. Multistable kirigami for tunable architected materials. Physical Review Materials 2 (11), 110601.
- [49] Yao, H., Gao, H., 2006. Mechanics of robust and releasable adhesion in biology: Bottom-up designed hierarchical structures of gecko. Journal of the Mechanics and Physics of Solids 54 (6), 1120–1146.
- [50] Yao, L., Alderliesten, R. C., Benedictus, R., 2016. The effect of fibre bridging on the Paris relation for mode I fatigue delamination growth in composites. Composite Structures 140, 125–135.
- [51] Yao, L., Alderliesten, R. C., Benedictus, R., 2016. The effect of fibre bridging on the Paris relation for mode I fatigue delamination growth in composites. Composite Structures 140, 125–135.
- [52] Ye, J., 2003. Laminated Composite Plates and Shells. Springer London, London.

[53] Zhao, N., Wang, Z., Cai, C., Shen, H., Liang, F., Wang, D., Wang, C., Zhu, T., Guo, J., Wang, Y., Liu, X., Duan, C., Wang, H., Mao, Y., Jia, X., Dong, H., Zhang, X., Xu, J., nov 2014. Bioinspired Materials: from Low to High Dimensional Structure. Advanced Materials 26 (41), 6994–7017.

Appendix A1: Reference specimens

To estimate the fracture toughness, \mathcal{G}_c , without the steady-state crack propagation (usually, after the crack onset, the crack kinked out of the path that was predesigned by etching) and the apparent bending rigidity EI, reference specimens with different initial crack lengths a=80, 100, 120 mm were prepared. Two specimens for each of the crack lengths were manufactured and tested. The laser cutting process used for manufacturing the specimens including the pre-crack yielded a crack of approximately 300 µm in width.

Apparent Bending Rigidity

Treating the specimens as cantilever beams, the compliance can be expressed with simple beam theory (ignoring the lower order Timoshenko beam effect, thus reflecting the apparent nature of estimated quantity), as:

$$C = \frac{a^3}{3EI} \tag{36}$$

From the experiments, the compliance of the specimens are measured as the tip displacement over the tip force $C_{exp} = \Delta/2P$. From eq. (36) the apparent bending rigidity of the specimens are obtained as:

$$EI = \frac{a^3}{3C_{exp}} = \frac{2Pa^3}{3\Delta} \tag{37}$$

Fig. 14 shows the measured force-displacement curves for specimens with three different crack lengths. By analyzing the initial, linear loading part of this data, the bending rigidity was found to be approximately $EI \approx 5.35$ N m² as an average value from all the experiments conducted.

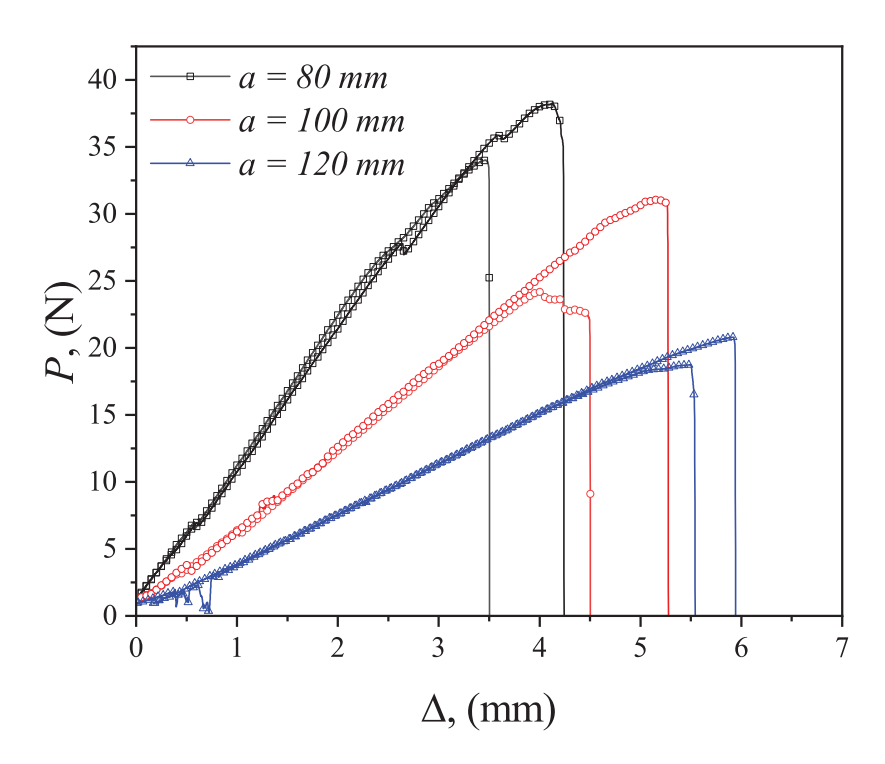


Figure 14: Experimental load response for the reference DCB specimens. Where the gray, red and blue lines represent an initial crack length of $80\,\mathrm{mm}$, $100\,\mathrm{mm}$ and $120\,\mathrm{mm}$, respectively.

Fracture Energy

To determine the fracture toughness of the material, the Irwin-Kies [11] method is used together with eq. (36) to obtain an expression for the energy release rate:

$$\mathcal{G} = \frac{P^2}{2b} \frac{dC}{da} \tag{38}$$

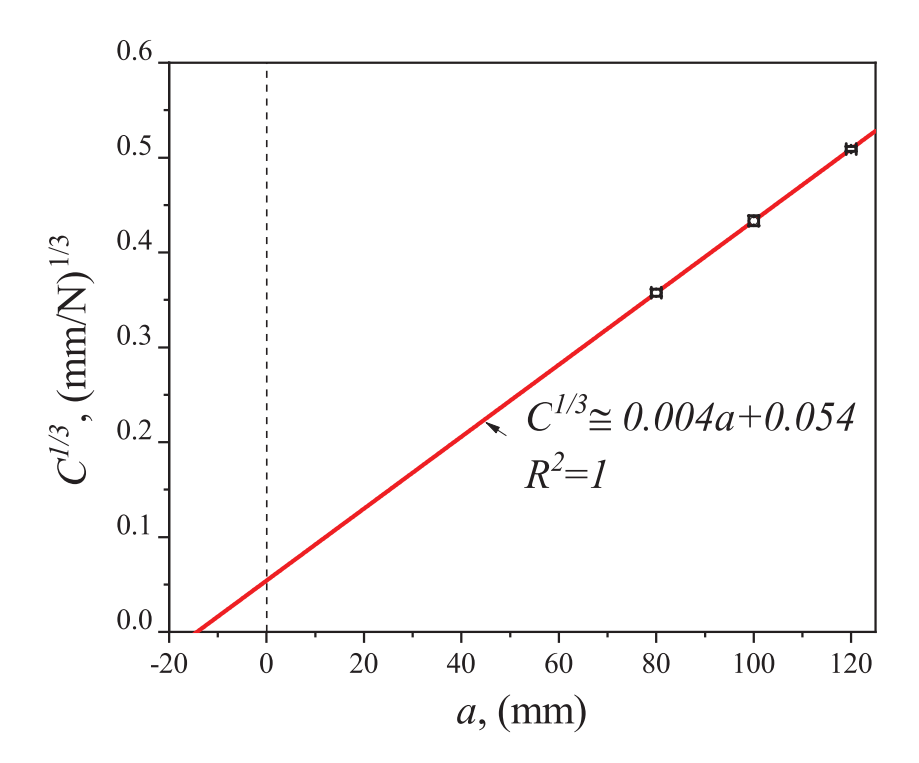


Figure 15: The experimental compliance plotted against initial crack length. The red line is a fit, presenting eq. (36), to the experimental data.

Two parameters, namely, the critical force at the crack onset P_c and the rate at which compliance changes with respect to growing crack, dC/da, are required for obtaining the fracture energy. The critical force is determined as the point where the linearity of the initial loading is lost. The reported, average, values are: $P_{c80} = 36.1 \text{ N}, P_{c100} = 27.6 \text{ N}, P_{c120} = 19.8 \text{ N}$. The second parameter is obtained by plotting the mean compliance for each of the crack lengths and fitting eq. (36) as $C = a_3 \cdot a^3$. In Fig. 15, the experimental data and the cubic fit are seen with the pre-factor $a_3 = 5.4787 \cdot 10^{-8}$. Note,

that the intersection point with the ordinate axis yields a positive value; this is due to the finite stiffness of the loading system and tested specimens (e.g. due to the process zone, root rotation effects or similar.) Finally, $\frac{dC}{da} = 3 \ a_3 \cdot a^2$ which together with eq. (38) and the critical forces yields a fracture energy $\mathcal{G}_c \approx 0.25 \ \text{N mm}^{-1}$, which is found in a very good agreement with available literature, e.g. [19, 6].

Appendix A2: Failure Due to Pillar Compression

While failure due to pillar compression was not observed in this work, the macro-mechanical solution implies existence of a compressive zone ahead the crack. For specific geometries and materials, the compressive loading may lead to collapse of the pillar by exceeding the compression strength or critical buckling load. To keep the analysis relatively short we assume that a single pillar can be treated as a beam under fixed-fixed boundary conditions at $z = \pm \frac{t}{2}$. For such case, the boundary conditions reads as $u(\pm \frac{t}{2}) = 0 \land \frac{du}{dz}(\pm \frac{t}{2}) = 0$. Assuming the pillar behaves as a slender beam, the buckling solution [9], leads to the critical (Euler) load:

$$P_c = 4EI_p \left(\frac{\pi}{t}\right)^2 \tag{39}$$

Assuming:

$$\sigma_{comp} = \frac{P_c}{bd} = 4E \frac{I_p}{bd} \left(\frac{\pi}{t}\right)^2 \tag{40}$$

with the radius of gyration $r = \sqrt{\frac{I_p}{bd}}$ one obtains:

$$\sigma_{comp} = \frac{1}{4} E \pi^2 \left(\frac{t}{r}\right)^{-2} \tag{41}$$

Taking, to the first approximation, eq. (23) we find:

$$\sigma_p = \sqrt[3]{4\frac{\mathcal{G}_c E^2}{t}} \tag{42}$$

which together with eq. (40) readily equates to the following non-dimensional criterion for compressive failure:

$$\left(\frac{d}{t}\right)^2 = c_1 \sqrt[3]{\frac{\mathcal{G}_c}{tE}} \tag{43}$$

with the non-dimensional constant $c_1 = \frac{\sqrt[3]{4}}{3\pi} \left(\frac{\sigma_{ccomp}}{\sigma_{cp}}\right)$ - index c corresponds to the failure stress. The structure fails in compression once the left hand side is greater than the right hand side. The buckling scenario could most likely take place once using brittle fibres and/or hair like structures. Such were not investigated here leaving place for the future exploration.